Electronic Supplementary Material (ESI) for Journal of Materials Chemistry C


*Supporting Information for:*

# Experimentally-Determined Intermediate Hydrocarbon Species Model of Atmospheric-Pressure Chemical Vapor Deposition of Graphene on Cu

Nathaniel S. Safron and Michael S. Arnold*

Department of Materials Science and Engineering, University of Wisconsin-Madison, Madison, WI 53706.

## I. Background:

For our analysis of the intermediate hydrocarbon species of graphene growth on Cu and the growth kinetics, we have chosen to model the nucleation and growth of graphene using a rate equation approach based on the work of Frenkel[1] and extended by Zinsmeister[2] (see reviews[3, 4]). The model is based on the arrival of a monomer precursor of growth to a surface, then using the mean concentration of monomer to estimate the nucleation rate of larger clusters and attachment of monomer to stable clusters. The rates are controlled by energetic differences in the species on the substrate surface, the kinetic barriers, and diffusivity of the different species. In principle, the concentration of *i*-sized clusters up to arbitrary size could be monitored. This analysis, however, would require *i*-coupled differential equations. Assumptions are necessary for both numerical analysis and analytical solutions.

It was noted by Zinsmeister[2] that clusters larger than a critical size are more likely to grow than decay, due to a reduction of the Gibbs free energy upon addition of more atoms. The number of clusters which reach this size can be assumed to grow into independent clusters, and their total number given by the integral of the nucleation rate, which can be monitored during the entire simulated growth. Additionally, necessary capture and decay rates from arbitrary sized clusters were formulated in terms of capture numbers.[5] These assumptions allow for the reduction from *i*-coupled differential equations for cluster concentrations to two, one for the monomer and one for the stable nuclei. Similar rate equations have been successfully used to model the growth of graphene on Ru.[6]

One stark contrast between our work and that of the early nucleation research is the types of growth species that are deposited. Early work focused on physical deposition where a flux of incoming metal atoms was set and the metal desorption rate was controlled by the temperature. Only a single elemental species needed consideration. Our work uses chemical vapor deposition, where the concentration of a precursor gas molecule is set and multiple breakdown reactions through intermediate hydrocarbons yield the production of hydrocarbon species of unknown composition that can attach to graphene. In CVD conditions, the nucleation of stable clusters is a difficult problem due to the unknown chemical composition of the stable nucleus and the multitude of reaction pathways that could yield this stable nuclei, thus more theoretical work is necessary. Therefore, we address nucleation

through our empirical evidence showing that the nucleation rate has a power law proportionality to the methane and hydrogen concentrations.

While there are many different hydrocarbon species on the surface, one hydrocarbon species is likely the primary source of carbon which can add to graphene, termed the "building unit" (BU) hydrocarbon, making the growth problem simpler as we only have to address the concentration of one hydrocarbon species. Which $C_xH_y$ species should this be? It must have a relatively high concentration (to have high reaction rates), have high diffusivity to reach the edges of graphene crystallites, and have a low kinetic barrier for the attachment to graphene. Due to the complexity of reaction schemes for methane decomposition for production of these hydrocarbons, we only consider simple reactions such as H additions and subtractions and hydrocarbon-hydrocarbons combinations and dissociations. In section III, we find the equilibrium concentrations, only considering methane desorption. In section IX, we consider the possibility of desorption of other hydrocarbons on the surface which can change the steady-state concentrations significantly from their equilibrium values.

## II. Diffusion of Gas through the Boundary Layer:

Typically, CVD processes are affected by the total flow rate in the system, sample position and orientation, and boundary layer phenomena. We measure the CMC while changing these process conditions at $T$=1000 °C and $[H_2]_{(g)}$=5% to identify if the phenomena we observe here are determined by processes that occur in the gas phase or on the Cu surface. We find that that the CMC is independent of lateral sample position along the tube (Fig. S3). Additionally, we find only small changes in the CMC (<10%) for different total flow rates (Fig. 2a) and (<10%) for different Cu foil orientations in the tube during the same growth conditions (Fig. S4). In the latter case, the highest final coverage is found for samples oriented perpendicular to the flow, followed by samples oriented parallel to the flow located on the inner surface of the process quartz tube wall, and least with samples oriented parallel to the flow located in the center of the flow raised above the tube wall. Nonetheless, the relative invariance in the data indicate that near the CMC, the net growth rate is sufficiently slow that surface, not gas phase, phenomena are most important. Because the CMC changes by <10% for different total flow rate and sample orientation and position, we treat these variations as secondary. Furthermore, there are minor morphological and Cu grain dependencies to the CMC. We find coverage highest on the top of ridges in the Cu foil and observe a small Cu grain dependence on final coverage, as well (Fig. S5); however, these effects also change the CMC by <10% and are therefore secondary, as well.

In atmospheric pressure CVD with constant flow of gas, a stagnant boundary layer of gas forms inside the tube and affects diffusion to the substrate. Adjacent to the quartz tube or substrate, friction between the gas and the surface creates a "no-slip" boundary condition where the gas velocity is zero at the surface. Therefore, if a gas component is being consumed by a substrate, its concentration near the surface may be different than in the convective gas flow far from the substrate, and can only be replenished by diffusion through the boundary layer. Additionally, hydrocarbon byproducts may be formed on the graphene-free Cu surface and subsequently desorb (see Section IX). These molecules may

either redeposit on the Cu surface or diffuse away into the gas stream, also influenced by the thickness of the boundary layer.

To experimentally test how diffusion of gas through the boundary layer affects growth, we changed the total flow rate (Fig. 2a) and Cu orientation in the tube (Fig. S4) and measured the CMC. We also modeled the boundary layer. The solution to the boundary-layer problem involves first solving the Navier-Strokes equation for the velocity profile of the gas inside the tube, then solving Fick's equation for the diffusion of the gas component (in this case methane) through the velocity profile to the substrate. We chose to model our precise set-up using Comsol software for different sample orientations and flow rates. Simulations were performed using the dynamic viscosity of Ar, 6.54 E-5 Pa·s, and the diffusion coefficient of $CH_4$ in Ar, 3.28 E-4 $m^2s^{-1}$, for $T$=1000 °C. The gas composition was set at the inlet of the quartz tube and the boundary condition at the surface set at a fixed concentration different from the gas inlet. The relative flux rate of methane to the center of each Cu foil is shown in Table 1 for the different flow rates and sample orientations: oriented perpendicular to the flow (PF), oriented parallel to the flow located on the inner surface of the process quartz tube (SF), and oriented parallel to the flow located in the center of the tube (CF) (sample orientations schematically shown in Fig. S4).

**Table 1:**

| Flow Rate (sccm) | PF $CH_4$ Flux (rel.) | SF $CH_4$ Flux (rel.) | CF $CH_4$ Flux (rel.) |
|---|---|---|---|
| 75 | 1.82 | 1.77 | 1 |
| 147 | 2.52 | 2.41 | 1.42 |
| 365 | 4.16 | 3.80 | 2.46 |
| 758 | 6.52 | 5.61 | 4.07 |

The simulated flux rate of methane to and from the sample varies by a factor of 6.5 over the experimental conditions. Therefore, if the methane concentration at the sample was far from equilibrium, we would expect the steady-state concentration near the Cu surface to be 6.5 times higher in the high flow PF case than in the low flow CF case. Since we only measure slight, <15%, changes in the CMC for these conditions, we believe that the methane concentration near the Cu surface is in fact very near equilibrium in all cases which results in small changes to the CMC for different boundary layer thicknesses.

## III. Equilibrium Hydrocarbon Concentration from the Precursor Gases:

Our first step in the solution to the BU species of graphene growth and growth kinetics is to find the concentration of different hydrocarbons on the Cu surface from the decomposition of methane and

hydrogen. Since, from the previous section, it appears the growth is near equilibrium, we find the equilibrium concentrations through the reaction of methane and hydrogen gases with the surface, only considering desorption of these two gases:

$$H_{2(g)} \leftrightarrow H_{2(s)}, CH_{4(g)} \leftrightarrow CH_{4_{(s)}}$$

For simplicity, we assume that the total coverage of all molecules is low, therefore reaction rates are independent of the total hydrogen and hydrocarbon species coverage. The methane reaction is assumed to be sequential as the carbon species loose successive hydrogen atoms. Additionally, hydrocarbons can combine and dissociate. The reactions take place as:

$$H_{2(s)} \leftrightarrow 2H_{(s)}, \qquad CH_{4(s)} \leftrightarrow CH_{3_{(s)}} + H_{(s)}, \;\; CH_{3(s)} \leftrightarrow CH_{2_{(s)}} + H_{(s)} \cdots, \qquad CH_{3_{(s)}} + CH_{3_{(s)}} \leftrightarrow C_2H_{6_{(s)}} \cdots$$

We assume the hydrogen reaction between the gas and surface dominates the amount of surface hydrogen ($n_H$), due to the fact that it is exothermic, has a small kinetic barrier, and has a much higher partial pressure in our experiments. For simplicity, all surface concentrations, *n*'s, are given in a unitless probability of occupation per area, normalized to the density of Cu lattice sites on the *graphene-free* Cu surface. The methane decomposition is sequential, with the rate of breakdown of one $CH_y$ species proportional to its concentration, the exponential of energy difference of the states plus the kinetic barrier. Its recombination with hydrogen is proportional to its concentration, the surface hydrogen concentration, and an exponential of just the kinetic barrier. The rate equations are:

$$\dot{n_H} \approx 2w_{H,H}\left(n_{H_2} - {n_H}^2 e^{\Delta E_{H_2}^{2H}\beta}\right) \qquad [1]$$

*1<y<3:*

$$\dot{n}_{CH_y} = w_{H,CH_y}\left(n_{CH_{y+1}} e^{-\Delta E_{CH_{y+1}}^{CH_y+H}\beta} - n_H n_{CH_y}\right) + w_{H,CH_{y-1}}\left(n_H n_{CH_{y-1}} - n_{CH_y} e^{-\Delta E_{CH_y}^{CH_{y-1}+H}\beta}\right) + 2w_{CH_y,CH_y}\left(n_{C_2H_{2y}} e^{-\Delta E_{C_2H_{2y}}^{2CH_y}\beta} - {n_{CH_y}}^2\right) \qquad [2]$$

$$\dot{n}_C = w_{H,C}\left(n_{CH} e^{-\Delta E_{CH}^{C+H}\beta} - n_H n_C\right) + 2w_{C,C}\left(n_{C_2} e^{-\Delta E_{C_2}^{2C}\beta} - {n_C}^2\right) \qquad [3]$$

where $\Delta E_{reactants}^{products}$ is the change in energy in the reaction, $w_{i,j}$ is the specific reaction rate per species concentration from its kinetic barrier(s), the values of $n_{H2}$ and $n_{CH4}$ are the probabilities of the precursor species at a Cu lattice site and constants for a given growth (at fixed gas concentrations and temperature), given by:

$$n_x = \frac{[X]_{(g)} s_{0,X} p}{\rho_{Cu} \nu_0 \sqrt{2 m_x k_B T}} \qquad [4]$$

where $[X]_{(g)}$ is the unitless concentration of precursor X in the gas phase adjacent to the surface, $s_{0,X}$ is the sticking coefficient of component X, $p$ is the total pressure of the chamber, $m_x$ is molecular weight of component $X$, $\rho_{Cu}$ is the density of Cu surface lattice sites, $\beta = 1/k_BT$, $k_B$ the Boltzmann constant, $T$ is the temperature, and $v_0$ the hopping frequency (~$10^{13}$ $s^{-1}$). It has been assumed for these equations that the hydrogen gas dissociation and carbon-carbon association reactions are exothermic while the hydrogen loss by hydrocarbons is endothermic.[7] Similar equations can be written for multi-carbon molecules.

The equilibrium surface concentrations are found when $\dot{n}=0$ and are given by:

$$n_H{}^0 = \sqrt{n_{H_2}}\, e^{-\Delta E_{H_2}^{2H}\beta/2}; \quad n_{C_xH_y}{}^0 = \frac{n_{CH_4}{}^x}{n_{H_2}{}^{(4x-y)/2}} e^{-(\Delta E_{xCH_4}^{C_xH_y+(4x-y)H} - \frac{4x-y}{2}\Delta E_{H_2}^{2H})\beta} \qquad [5]$$

These values are constants for a given growth and represent the equilibrium concentrations from the methane gas. They are related to the partial pressure of hydrogen and methane and can thus be changed experimentally.

## IV. Rate equations for Graphene Growth and Nucleation from $C_xH_y$:

Next, continuing our analysis of the possible intermediates and reaction kinetics, we derive the necessary rate equations. Assuming the growth and etching can be related to just one species, we can write the rate equation for the BU concentration ($n_{C_xH_y}$) and total coverage ($Z$):

$$\dot{n}_{C_xH_y} = R_V\left(n_{C_xH_y}{}^0 - n_{C_xH_y}\right) - \frac{\nu_0(n_{C_xH_y} - n_G{}^0)}{1-Z}\sum_{i=1}^{n_s}\sigma_{s,i} \qquad [6]$$

$$\dot{Z} = \nu_0(n_{C_xH_y} - n_G{}^0)\sum_{i=1}^{n_s}\sigma_{s,i} \qquad [7]$$

The two terms in Eq. 6 are the creation and dissociation of $C_xH_y$ through intermediates from the methane, and hydrocarbon attachment and detachment from stable graphene nuclei, respectively. The steady-state concentration $n_{C_xH_y}{}^0$ could be the equilibrium concentration in Eq. 5 or could deviate from that value (see Section IX). The rate equation of Z is the net rate of hydrocarbon addition and subtraction to stable graphene crystallites. $R_V$ is rate of $C_xH_y$ formation and breakdown from other hydrocarbons, $n_s$ is the time-dependent stable nuclei concentration, $n_G{}^0 = e^{\Delta E_{C_xH_y}^{xC_{graphene}+yH}\beta}$ is the equilibrium concentration of the $C_xH_y$ from graphene, discussed further in Section VIII, and $\sigma_s$ is the capture number which approximates the probability of capture:

$$\sigma_s{}^{-1} = \sigma_B{}^{-1} + \sigma_D{}^{-1} \qquad [8]$$

where $\sigma_s$ is the inverse sum of the capture numbers due to diffusion ($\sigma_D$) and attachment ($\sigma_B$), the smaller of which will limit growth. The diffusion capture number is:

$$\sigma_D \approx \frac{\pi q_s}{2\lambda} e^{-E_D\beta}\, K_1(\frac{q_s}{\lambda})/K_0(\frac{q_s}{\lambda}) \quad [9]$$

where $q_s$ is the radius of the cluster s, $K_X$ are *x*-order modified Bessel functions of the 2nd kind, $E_D$ is the diffusion barrier of $C_xH_y$, and $\lambda$ is the average diffusion distance of $C_xH_y$ in a particular direction before chemical conversion given by $\lambda = \left(\nu_0 e^{-E_D\beta} {R_V}^{-1}\right)^{1/2}$. The attachment capture number is:

$$\sigma_B \approx 2\pi q_s e^{-E_B\beta} \quad [10]$$

where $E_B$ is the attachment barrier of $C_xH_y$. These equations were derived from p. 65-71, 73-78 in Ref. 3, where we have modified the creation of $n_{C_xH_y}$ from $CH_4$ decomposition for CVD conditions (discussed in Section III) instead of physical vapor deposition.

Our interest is to evaluate the growth at low coverage, before graphene crystallites grow into each other and stitch together, which reduces the edge area for attachment of further hydrocarbons. Therefore, Eq. 6 and 7 do not include the reduction of edge sites due to crystallites merging, which we could not incorporate into the rate equations.

Nucleation is assumed to have a power-law proportionality to the $n_{C_xH_y}$ species concentration, as found experimentally, and have an associated formation energy. This proportionality can be understood through classical nucleation theory, which dealt with typically single atoms arriving at a fixed flux and forming elemental clusters, and describes the formation of large but sub-critical clusters through first order kinetics and a linear reaction chain. The concentration of these clusters ($n_i$) quickly thermalize under the Walton relation[8] to their equilibrium values based on the concentration of a monomer ($n_1$): $n_i \propto {n_1}^i e^{-\Delta E_{in_1}^{n_i}\beta}$. The rate of a cluster growing to a stable size (at $i=i^*$), is proportional to $n_1 \cdot n_{i-1}$, or $\propto {n_1}^{i^*}$. However, due to the multiple reaction species and pathways in graphene CVD, we cannot assume the same first-order kinetics and linear reaction chain. Therefore, we write the rate equation for stable nuclei, to empirically match to data, as:

$$\dot{n_s} = w_{nuc} {n_{C_xH_y}}^{i^*} e^{-E_F\beta}(1-Z) \quad [11]$$

where $w_{nuc}$ the nucleation capture rate, and $E_F$ is the formation energy of the cluster prior to nucleation,. While the event of nucleation will deplete some of the $C_xH_y$ species from the surface, the rate is much smaller than the other rates, and is negligible in Eq. 6. $n_s$ is the only surface concentration that is given as the concentration on the *total surface area*, not the *graphene-free surface area* as all other surface concentrations are defined.

## V. The Critical Methane Concentration:

As shown in Fig. 2c of the manuscript, we have experimentally determined that the CMC $\propto {[H_2]_{(g)}}^{3/2}$. To determine what this data can tell us about the possible hydrocarbon intermediate, we examine the Eqs. 6 and 7 to find the condition of the critical methane concentration. From Eq. 6, we see

that the first term reaches its steady-state value when $n_{C_xH_y} = {n_{C_xH_y}}^0$. From Eq. 7 for the total graphene coverage, the condition for no graphene growth or etching is $n_{C_xH_y} = {n_G}^0$, below which no graphene can grow. ${n_{C_xH_y}}^0$ is adjusted by changing the methane or hydrogen partial pressures while ${n_G}^0$ is fixed by energetics (see Section VIII for discussion on Hydrogen Etching). Therefore, the critical methane concentration is found when ${n_{C_xH_y}}^0 = {n_G}^0$. Noting that, for the experimental condition of the CMC $\propto [H_2]_{(g)}^{3/2}$, the species $C_xH_y$ must have x=y, we solve for the critical methane concentration for any $C_xH_x$ intermediate under equilibrium conditions (Eq. 5):

$$CMC = \frac{([H_2]_{(g)} s_{0,H_2})^{3/2} \sqrt{p\, m_{CH_4}}}{s_{0,CH_4} \left(\rho_{Cu} \nu_0 \sqrt{2 {m_{H_2}}^3 k_B T}\right)^{1/2}} e^{(\Delta E_{CH_4 + Cu_{surf}}^{C_{graphene} + 4H + Cu_{surf+graphene}})\beta} \quad [12]$$

where we have cancelled the energetics of the intermediates.

Other hydrocarbon species may take part in graphene growth. For instance, atomic C on the surface likely could grow graphene. However, its surface concentration may be much lower than $C_xH_x$ that it has only a small effect. A $CH_2$ species may take part in growth, but could have a low diffusivity or high barrier for attachment to graphene, making its attachment rate much smaller. We cannot assess these secondary reactions from our data that finds a $C_xH_x$ intermediate as the BU species.

## VI. Derivation of Analytic Equations for Growth and Nucleation:

To solve these rate equations for comparison with the kinetic experiments shown in Fig. 3 in the manuscript, we make several approximations and look at the limiting cases. Since we are only looking at the beginning stages of growth, we can make the approximation that (1-*Z*) ≈1. We also approximate the radius of the growing graphene nuclei as the equal-radius average, $q_s \approx (Z/n_s\pi)^{1/2}$, which allows us to replace the summation over the capture numbers of different nuclei with their average value. Equations 6, 7, and 11 are approximated as:

$$\dot{n}_{C_xH_y} \approx R_V \left({n_{C_xH_y}}^0 - n_{C_xH_y}\right) - \nu_0 \sigma_s n_s (n_{C_xH_y} - {n_G}^0) \quad [13]$$

$$\dot{Z} \approx \nu_0 \sigma_s n_s (n_{C_xH_y} - {n_G}^0) \quad [14]$$

$$\dot{n}_s \approx w_{nuc} {n_{C_xH_y}}^{i^*} e^{-E_F \beta} \quad [15]$$

The Limiting Cases for Species Concentration:

The first equation can then be solved for $n_{C_xH_y}$ at the steady-state ($dn_{C_xH_y}/dt$=0).

$$n_{C_xH_y} = \frac{R_V {n_{C_xH_y}}^0 + \nu_0 \sigma_s n_s {n_G}^0}{R_V + \nu_0 \sigma_s n_s} \quad [16]$$

This equation can be simplified in either of the limiting cases:

$$R_V {n_{C_xH_y}}^0 \gg \nu_0 \sigma_s n_s {n_G}^0 \; yields \; n_{C_xH_y} = {n_{C_xH_y}}^0$$

$$R_V {n_{C_xH_y}}^0 \ll \nu_0 \sigma_s n_s {n_G}^0 \; yields \; n_{C_xH_y} = {n_G}^0$$

These equations describe the real-time value of $n_{C_xH_y}$ during the growth. The first limit is the "capture-limited concentration" (CLC) regime since the rate of incoming carbon from the vapor is much higher than its capture from graphene, and $n_{C_xH_y}$ is equal to the vapor steady-state concentration, ${n_{C_xH_y}}^0$, and therefore increases as $[CH_4]_{(g)}$ is increased. The second limit is the "adsorption-limited concentration" (ALC) since the rate of capture by graphene is much greater than the rate of incoming carbon from the vapor, all excess $C_xH_y$ will attach to graphene leaving $n_{C_xH_y}$ equal to the graphene dissociation equilibrium concentration, ${n_G}^0$.

The Limiting Cases for Capture:

Capture itself has two limiting cases described by Eq. 9 for the diffusion capture number. During the growth, we approximate the radius of the growing graphene nuclei as the equal-radius average, $q_s \approx (Z/n_s\pi)^{1/2}$. If $\sigma_D$ limits the growth rate and the relationship between $q_s$ and the average diffusion distance, $\lambda = \left(\nu_0 e^{-E_D\beta} {R_V}^{-1}\right)^{1/2}$, is consistent for the whole growth, than this equation can be simplified in either of the limiting cases:

$$q_s \gg \lambda \; yields \; \sigma_D \approx 2\pi q_s e^{-E_D\beta}/\lambda$$

$$q_s \ll \lambda \; yields \; \sigma_D \approx 2\pi e^{-E_D\beta}/ln(\lambda/q_s) \approx constant$$

Always, $\sigma_B$ is proportional to the radius of the graphene cluster, functionally similar with the first case.

The first case is termed "linear capture" (LC) since growth is proportional to the perimeter of the growing graphene crystallites. Practically, this case occurs if the average diffusion distance is low compared to the distance between graphene crystallites *or* there is a high attachment barrier, therefore, hydrocarbon attachment will be proportion to the number of edge sites on each graphene crystallite. The second case is "constant capture" (CC) and occurs if the average diffusion length is much longer than the radius of the graphene *and* there is a small attachment barrier. The capture number is approximately constant for any size cluster, since almost all excess hydrocarbon species that form will be captured.

Analytical Solutions of Growth Equations:

The surface concentration can be determined by two cases and the capture can be defined by two cases, so in total we have 4 cases. The strategy of solving the two remaining equations is first noting that $\dot{n_s}$ is constant in all cases since $n_{C_xH_y}$ is constant, so $n_s(t) = \dot{n_s}t$. Then, we integrate $\dot{Z}$ and solve for the time when $Z$ is at half coverage, ($t=t_c$), with the approximations given above for each case. Finally, we use this time to find the stable nuclei concentration at half coverage, denoted as $N_S$, which is equal

to $\dot{n}_s t_c$. In the case of adsorption limited capture where $n_{C_xH_y} \approx {n_G}^0$, $(n_{C_xH_y} - {n_G}^0) \approx R_V({n_{C_xH_y}}^0 - {n_G}^0)/\nu_0\sigma_s n_s$ (approximated from Eq. 16) and the capture term, $\nu_0\sigma_s n_s$, cancels from the equation of $\dot{Z}$ resulting in both ALC capture types having the same dependencies.

Constant Rates for Each Case:

Each of the resulting three limiting cases (CLC with LC, CLC with CC, and ALC with LC or CC) will have a specific growth rate ($R_{constant}$) which is constant during the whole growth. For CLC with LC, the radial growth rate of each crystallite is constant because the crystallite's total capture is proportional to its circumference. We can calculate the radial growth rate $R_{radial} = w_{radial}({n_{C_xH_y}}^0 - {n_G}^0)$, where $w_{radial} = \nu_0/2\pi\left[\left(\frac{\nu_0}{4}e^{E_D\beta}{R_V}^{-1}\right)^{1/2} + e^{E_B\beta}\right]^{-1}$. For CLC with CC, the total growth of each crystallite is constant, therefore $R_{crystal} = \nu_0\sigma_s({n_{C_xH_y}}^0 - {n_G}^0)$, with $\sigma_s = 2\pi e^{-E_D\beta}/ln(\lambda/q_s)$, approximately constant. For ALC with either capture, the total coverage rate is constant during the growth as an increase in $\sigma_s$ or $n_s$ reduces $(n_{C_xH_y} - {n_G}^0)$ further, resulting in the total coverage rate $R_{coverage} = R_V({n_{C_xH_y}}^0 - {n_G}^0)$. In all cases, the nucleation rate $R_{nuc} = w_{nuc}(n_{C_xH_y})^{i^*}e^{-E_F\beta}$ is the same, where in CLC: $n_{C_xH_y} = {n_{C_xH_y}}^0$ and in ALC: $n_{C_xH_y} = {n_G}^0$. In practice, these rates are only valid for low coverage while the (1-$Z$) ≈1 approximation holds and before different graphene crystallites begin stitching together. Using these analytic equations for $t_c$ and $N_S$, we can solve for the constant growth rate and nucleation rate in each case in terms of these experimentally measured values. Additionally in Table 2, we show the proportionality between each measured value (at a single temperature) and the external parameters ($[CH_4]_{(g)}$, $[H_2]_{(g)}$, and the CMC, which itself depends on $[H_2]_{(g)}$) for the CH species determined in by our data. We also show the initial dependence of coverage on growth time, $t$. The results are summarized in Table 2:

Table 2.

| Regime | $t_c$ | $N_S$ | $R_{constant}$ | $R_{nuc}$ | $Z$ |
|---|---|---|---|---|---|
| CLC, LC | $(9/8\pi)^{1/3}(w_{radial}\Delta n)^{-2/3}R_{nuc}^{-1/3}$ | $(9/8\pi)^{1/3}(w_{radial}\Delta n)^{-2/3}R_{nuc}^{2/3}$ | $w_{radial}\Delta n = (9/8\pi N_S)^{1/2}t_c^{-1}$ | $R_{nuc} = N_S/t_c$ | |
| ∝ | $([CH_4]\text{-}CMC)^{-2/3}\cdot[CH_4]^{-i^*/3}\cdot[H_2]^{(i^*/2+1)}$ | $([CH_4]\text{-}CMC)^{-2/3}\cdot[CH_4]^{2i^*/3}\cdot[H_2]^{(1-i^*)}$ | $([CH_4]\text{-}CMC)\cdot[H_2]^{-3/2}$ | $[CH_4]^{i^*}\cdot[H_2]^{-3i^*/2}$ | $t^3$ |
| CLC, CC | $(\sigma_s\nu_0\Delta n)^{-1/2}R_{nuc}^{-1/2}$ | $(\sigma_s\nu_0\Delta n)^{-1/2}R_{nuc}^{1/2}$ | $\sigma_s\nu_0\Delta n = (N_S t_c)^{-1}$ | $R_{nuc} = N_S/t_c$ | |
| ∝ | $([CH_4]\text{-}CMC)^{-1/2}\cdot[CH_4]^{-i^*/2}\cdot[H_2]^{3/4(i^*+1)}$ | $([CH_4]\text{-}CMC)^{-1/2}\cdot[CH_4]^{i^*/2}\cdot[H_2]^{3/4(1-i^*)}$ | $([CH_4]\text{-}CMC)\cdot[H_2]^{-3/2}$ | $[CH_4]^{i^*}\cdot[H_2]^{-3i^*/2}$ | $t^2$ |
| ALC, LC or CC | $(2R_V\Delta n)^{-1}$ | $R_{nuc}(2R_V\Delta n)^{-1}$ | $R_V\Delta n = (2t_c)^{-1}$ | $R_{nuc} = N_S/t_c$ | |
| ∝ | $([CH_4]\text{-}CMC)^{-1}\cdot[H_2]^{3/2}$ | $([CH_4]\text{-}CMC)^{-1}\cdot[CH_4]^{i^*}\cdot[H_2]^{3/2(1-i^*)}$ | $([CH_4]\text{-}CMC)\cdot[H_2]^{-3/2}$ | constant | $t$ |

with $\Delta n$ as the difference in steady-state species concentrations: $({n_{CH}}^0 - {n_G}^0)$, $i^*$ the nonlinearity coefficient of the nucleation rate (found to be 2.65), and the growth regime determined to be CLC with LC.

## VII. Supplementary Experimental Data and Comparison with Modeling of the Intermediate Growth Regimes:

In Fig. S6a, we plot the $t_c$ and $N_S$ data for $[H_2]_{(g)}$=2.5%, 10% and 20%. In Fig. S6b, we plot the radial growth rate at $[H_2]_{(g)}$=2.5, 5 and 10 % as a function of $[CH_4]_{(g)}$ on a linear-linear plot to clearly show the observed linear dependence of growth on BU supersaturation. Best fit lines were determined by a sum of squares of the log of the residual, sum((log(data)-log(fit))$^2$), to equally weight all data points. Also one data point for $[H_2]_{(g)}$=2.5% at GR=163 nm/s and $[CH_4]_{(g)}$ = 203ppm is cut out at the displayed range. The intercept from the linear fits, showing the etching rate of graphene at $[CH_4]_{(g)}$ = 0, is nearly the same from all fits. In Fig. S6c, we plot our growth rate data with other AP-CVD growths at $T$=1000°C from the literature, where we have analyzed the radial growth rate in the same manner that we do for our data (from $N_S$ and $t_c$). These growths ranged in [H2] from .8% to 25%. There is a large scatter in the growth rates from different groups, where we have good agreement with the work of Luo et al. Since our model can clearly predict our growth rate data at different [H2], we think the differences in the experimental growth rate can occur because 1) different annealing conditions before growth, which can affect the smoothness of the surface, and 2) different purity and/or facets in the Cu foil, all of which can affect the diffusion and attachment barriers in $w_{radial}$ in the growth rate formula. Additionally, other factors include 3) the specific CVD system geometry and flow rates, which can affect the diffusion of CH4 to the surface in growths with $[CH_4]$>>CMC, 4) the exact temperature, which affects all reaction rates, and 5) a potentially different concentration of impurities in precursor gases, which could change the CMC if the impurity concentration was high enough. Also, we calculate $t_c$ by subtracting the time that it takes for the $CH_4$ to reach the sample in the flow stream (approximately 2 min in our set-up). Other groups likely do not adjust their growth time for this factor, which will affect the calculated growth rate significantly for short growth times (two of which are < 5 min, which could affect the measured growth rate by > 40% for our geometry).

Our goal is to evaluate our kinetic data shown in Fig. 3 of the manuscript on the effect of methane concentration at fixed $T$ on $t_c$, $N_S$, $R_{radial}$, and $R_{nuc}$ to our model's predictions. For our data, we get a very good correlation to the nucleation rate (Fig. 3d) in the CLC regime for $\Delta E_{CH}^{C_{graphene}+H}$=-1.65 eV[9] and $i^*$=2.65 with $w_{nuc}e^{-E_F\beta} = v_0 e^{-4.0eV\beta}$. Linear capture, indicated by the linear dependence on $R_{radial}$ on the BU supersaturation (shown Fig. 3c), could be the result of diffusion or attachment limited capture, and defining $R_V = v_0 \exp(-K_A\beta)$ , we find good agreement with the data for $K_A + E_D$=1.1 eV for diffusion-limited capture or $E_B$=0.55 eV for attachment-limited capture. For the diffusion limited case, in order to guarantee that λ is small for the whole growth, $K_A \leq E_D$, in agreement with the DFT calculation of the kinetic barrier of $K_A$=0.5 eV for the $CH_{2(s)} \leftrightarrow CH_{(s)} + H_{(s)}$ reaction on Cu (100), which is a good candidate for the dominant reaction producing CH.[7] We cannot find DFT values for the diffusion barrier

or attachment barrier for CH, however the attachment barrier is in reasonable agreement with the DFT calculation of C attachment with a Cu adatom catalyst of $E_B$=0.8 eV.[10]

The intermediate capture regime:

In this case, $q_s \ll \lambda$ at the beginning of growth when the nuclei are small and the capture is constant. As the nuclei grow, the growth will transition to linear capture. The difference between the two is most easily found in the dependence of $R_{radial}$ on $S$, which follows a ~$N_S^{-1/2}t_c^{-1}$ trend in LC and a ~$N_S^{-1}t_c^{-1}$ in CC.

We have modeled the growth using equations 6, 7, and 11 using the average nuclei size approximation, $q_s \approx (Z/n_s\pi)^{1/2}$, get better insight. We have simulated the same conditions as previously, except with a constant $K_A$=0.5 eV and $E_B$=0 eV, with $E_D$ changing in the range of 0 to 1.2 eV. Figure S7a shows the results of the model for $R_{radial}$ ~$N_S^{-1/2}t_c^{-1}$, shown with the data from in Fig. 3c with $[H_2]_{(g)}$=5% in the manuscript. With low $E_D$, the average diffusion distance is much larger than the crystallites, which results in CC and non-linear $R_{radial}$. As $E_D$ increases, the diffusion distance becomes smaller, and growth becomes proportional to the circumference of the crystallite, resulting in a linear $N_S^{-1/2}t_c^{-1}$ for higher $E_D$ values. The LC fit describes the data better than the CC fit evidenced by its coefficient of determination, which has a 5 times better p-value.

The intermediate concentration regime:

In this case, $R_V {n_V}^0 \gg w_{1s} n_s {n_G}^0$ at the beginning of growth (when there is a small stable nuclei concentration) and the $n_{C_xH_y} \approx {n_{C_xH_y}}^0$ approximation is valid. Once sufficient nuclei have formed, the surplus carbon species is consumed by the growing nuclei and $n_{C_xH_y}$ reduces to ${n_G}^0$. In cases where the methane concentration is much higher than the critical value, much nucleation occurs during the early transient where $n_{C_xH_y}$ is high, since nucleation is proportional to ${n_{C_xH_y}}^{i^*}$. Simulations show that this early transient nucleation can dominate the total $N_S$ for the higher supersaturations implemented in this study and therefore modeling is necessary to get accurate results.

In this simulation, capture has been set in the code to be linear with $E_B$=0 eV and $E_D$ =0.05 eV, while $K_A$ is varied in the range 1.0 to 2.6 eV. The effect of changing $K_A$, and therefore $R_V$, is to change the rate of adsorption to be much faster than capture (CLC at $K_A$=1.0 eV) or much slower than capture (ALC at $K_A$=2.6 eV). Figure S7b shows the results of $R_{nuc}=N_S/t_c$. In the intermediate case, $R_{nuc}$ changes during the growth as $n_{C_xH_y}$ decreases throughout the growth. The plots represent the time-averaged value of the rates and are evaluated how we have experimentally determined the rates in the manuscript (from $t_c$ and $N_S$). For ALC ($K_A$=2.6 eV), $R_{nuc}$ has a much smaller dependence on $[CH_4]_{(g)}$. These simulations show that $R_{nuc}$ can have a power-law dependence on $[CH_4]_{(g)}$ at the onset of the transition from CLC, which slightly reduces the extracted $i^*$. The deviation of the nucleation rate at $[H_2]_{(g)}$ = 2.5% compared to other $[H_2]_{(g)}$ measured here may be due to the onset of interplay for the kinetically limiting step, small incorporation of $O_2$ impurities which have been shown to lower graphene nucleation,[11] or other factors. Further simulation and experiment on the nucleation reaction is necessary to determine its mechanism. Figure S7c shows the results of the model for $R_{radial}$ ~$N_S^{-1/2}t_c^{-1}$, shown with the data with $[H_2]_{(g)}$=5% in Fig.

3c in the manuscript. For ALC ($K_A$=2.6 eV), the radial growth rate clearly deviates from linear, due to the depletion of excess hydrocarbons, and thereby changes as a function of time during the growth, resulting in constant $R_{coverage} \sim t_c^{-1}$.

## VIII. Hydrogen Etching of Graphene:

In the manuscript and Section V of the Supporting Information, we derive the condition of the critical methane concentration under the assumption that the etching rate of the BU from graphene is independent of the surface hydrogen concentration. However, if CH is the etching species, the etching will necessitate hydrogen for removal of C from graphene. We considered the possibility that etching is limited by the diffusion of H to the graphene edge to remove carbon atoms from graphene. In that case, the equilibrium concentration from the solid would be:

$$n_{G,H\ case}{}^0 = n_H{}^0 e^{\Delta E_{CH}^{C_{graphene}+H}\beta} \propto \sqrt{[H_2]_{(g)}} \qquad [17]$$

If this was the case, CMC $\propto [H_2]_{(g)}^2$, indeterminate of the type of reactant species, which is not found experimentally.

We hypothesize that, since there is a 0.5 eV adsorption energy for hydrogen bonded to a graphene zigzag edge compared to hydrogen bonded to the Cu surface,[12] the graphene edge is saturated with H atoms and that when a hydrocarbon is removed from graphene it takes the hydrogen atom with it. The new graphene edge can be re-saturated by H at some short time later. In that case, as long as the surface hydrogen was not so low that reattachment of hydrogen to the graphene edge is rate-limiting, we would expect $n_G{}^0$ to be independent of $[H_2]_{(g)}$ as in all previous equations. This finding can be seen by the following two-step reaction for the radial etch rate of graphene by H. Step 1 is H attaching to graphene at rate $k_1$ and detaching at rate $k_{-1}$. Step 2 is a hydrocarbon detaching at rate $k_2$. The rate equation of percentage of hydrogen occupied sites is:

$$\dot{\theta} = k_1 n_H{}^0 (1-\theta) - k_{-1}\theta - k_2\theta$$

The percent of hydrogen occupied graphene edge sites can be found at steady-state ($\dot{\theta} = 0$):

$$\theta = \frac{k_1 n_H{}^0}{k_1 n_H{}^0 + k_{-1} + k_2}$$

Saturated hydrogen coverage, $\theta \approx 1$, implies that $k_1 n_H{}^0 \gg k_{-1}, k_2$. From the energetics, we can estimate $k_1 / k_{-1} \sim 100$ at $T$=1000 °C . Additionally, $k_1 / k_2$ is likely even larger since CH is energetically unfavorable on the Cu surface.[7, 10] Therefore, as long as $n_H{}^0 \geq 2\%$, the graphene edge is mostly saturated with H atoms. Our equilibrium equation (Eq. 5) for yields $2.4\% < n_H{}^0 < 9.3\%$ for the range 2.5% < $[H_2]_{(g)}$ < 40% for $s$=1, in agreement. The hydrocarbon etching reaction rate can be found as $k = \theta k_2 \approx k_2$, independent of $n_H{}^0$. The effect of H saturation on the attachment barrier of CH and other hydrocarbons to graphene should be addressed in future theoretical studies.

## IX. Effect of Desorption on the Steady-State Hydrocarbon Concentrations:

To discuss the validity of our equilibrium hydrocarbon model discussed in the manuscript and previous sections leading to CH as the BU species, we simulate the effect of desorption on the steady-state concentrations of hydrocarbons on the Cu in this section. Zeigarnik and coworkers[13] have described the energetics of $C_xH_y$ species up to *x*=2 on Cu(111) using a semi-empirical unity bond index - quadratic exponential potential (UBI-QEP) method including 15 species: $CH_4$, $CH_3$, $CH_2$, CH, C, $CH_3$- $CH_3$, $CH_3$- $CH_2$, $CH_3$- CH, $CH_3$- C, $CH_2$- $CH_2$, $CH_2$- CH, $CH_2$- C, CH- CH, CH- C, and $C_2$. The formation energy of each species can be found by comparing the gas-phase bond strengths and the binding energy to Cu(111) with those of methane and hydrogen. Each species can undergo H attachment and detachment, mono-carbon combination to a bi-carbon species, and bi-carbon species dissociation. The kinetic barrier of these reactions is unknown, but will involve a diffusion barrier of H in the H reactions and the diffusion of a hydrocarbon species for mono-carbon combination, as well as the attachment barrier due the transient state in the chemical reaction. Additionally, desorption will have a kinetic barrier. For modeling, we find the H concentration and monitor the rate equations of each hydrocarbon species similarly to Section III, expect that we include a desorption rate for each species based on a kinetic barrier and the binding energy. Since we do not know the kinetic barriers, we set the surface reaction kinetic barrier each be 1 eV, then vary the desorption barrier from 0 to 3 eV to see the effect of desorption. We have modeled each of our three experiment types: changing $[CH_4]_{(g)}$ at fixed $[H_2]_{(g)}$=5% and *T*=1000 °C, changing $[H_2]_{(g)}$ at *T*=1000 °C and $[CH_4]_{(g)} \propto [H_2]_{(g)}^{3/2}$, and changing temperature at $[H_2]_{(g)}$=5% and constant $[CH_4]_{(g)}$, shown in Figs. S8, respectively, where results of CH and C-CH are shown in a-c) and d-f), respectively.

For a large desorption kinetic barrier, the results corroborate our equilibrium calculations due to the desorption rate being negligible. However, for the lower desorption kinetic barriers, even though the desorption of CH is negligible due to its high binding energy of ~3eV, the surface concentration of CH can change significantly from the equilibrium values at each condition. Additionally, its dependency on the experiment conditions can change from Eq. 5. We have found that for the desorption barrier range of 0.5-1.5 eV, C-CH can follow the same trends as CH in the equilibrium case for the first two experimental conditions (Fig. S8 d+e). The Arrhenius dependence for these desorption barrier in Fig. S8 f is significantly different from its equilibrium dependence by ~0.6 eV. Therefore we would expect, if these kinetic were correct, the Arrhenius temperature of the critical methane concentration to be approximately $\propto e^{0.02eV\beta}$, which is significantly different from what we measure experimentally ($e^{0.51eV\beta}$).

The point of these simulations and discussion in this section is not to find the correct species for graphene growth. We have made many assumptions and simplifications to the problem in the kinetic barriers. Additionally, DFT calculations of the binding energies of $CH_y$ species and $C_2H_2$ differ considerably from those in this UBI-QEP method,[7, 14] and should be the subject of future study. The goal of this section is to show how desorption can affect the equilibrium concentration of other species (for

instance C-CH), which can result the same dependency of surface concentrations that we have found for the BU species in AP-CVD.

## X. Supporting Figures:

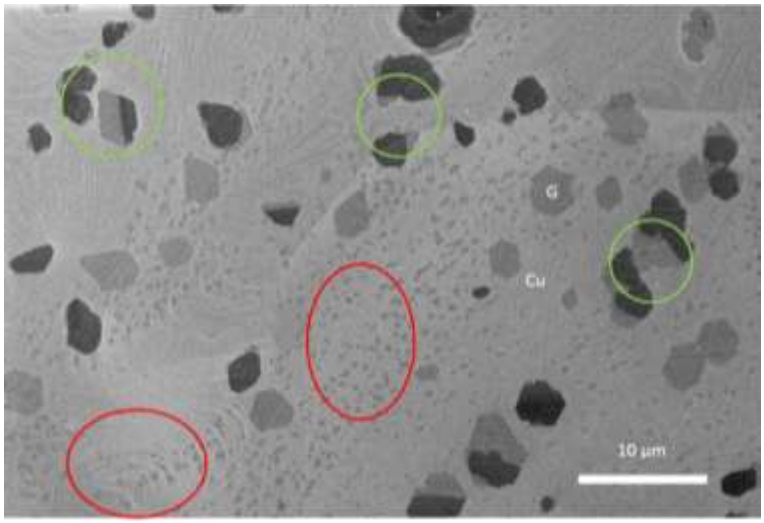


Figure S1. PC substrate (with partial growth at 1020 °C) followed by near CMC growth (27 ppm $CH_4$) at 925 °C. Green circles indicate initial nuclei from the PC substrate that are intact after second growth, while red circles indicate new nuclei during the second growth.

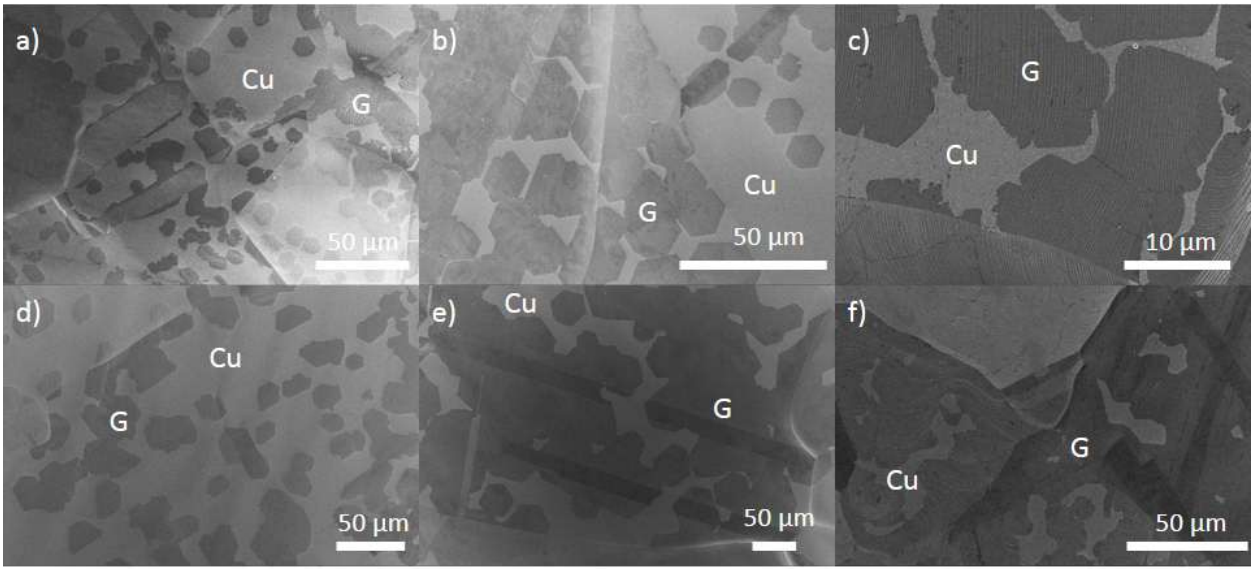


Figure S2. a-c) Growth (18 ppm $CH_4$) without $H_2$ purifier at atmospheric pressure and *T*=1000 °C of original a) NC, b) PC, and c) FC substrates. d-f) Identical growth with $H_2$ purifier at (atmospheric pressure +10 torr) of original d) NC, e) PC, and f) FC substrates. The CMC of all samples is 18 ppm.

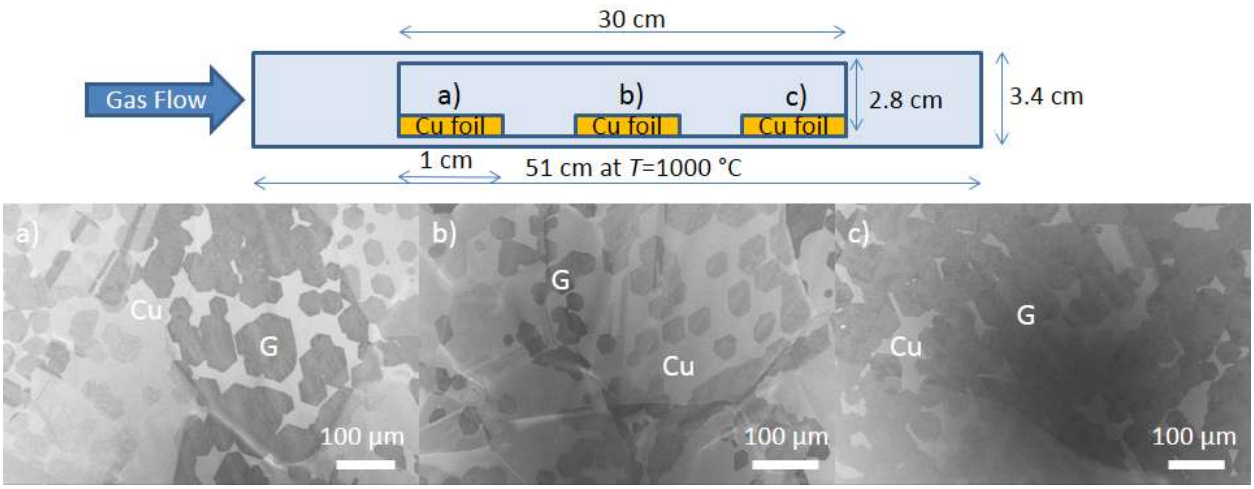


Figure S3. Positional dependence of growth (18 ppm $CH_4$) at atmospheric pressure and *T*=1000 °C for a) upstream, b) middle, and c) downstream positions on inner surface of quartz sleeve. The CMC of all samples is 18 ppm.

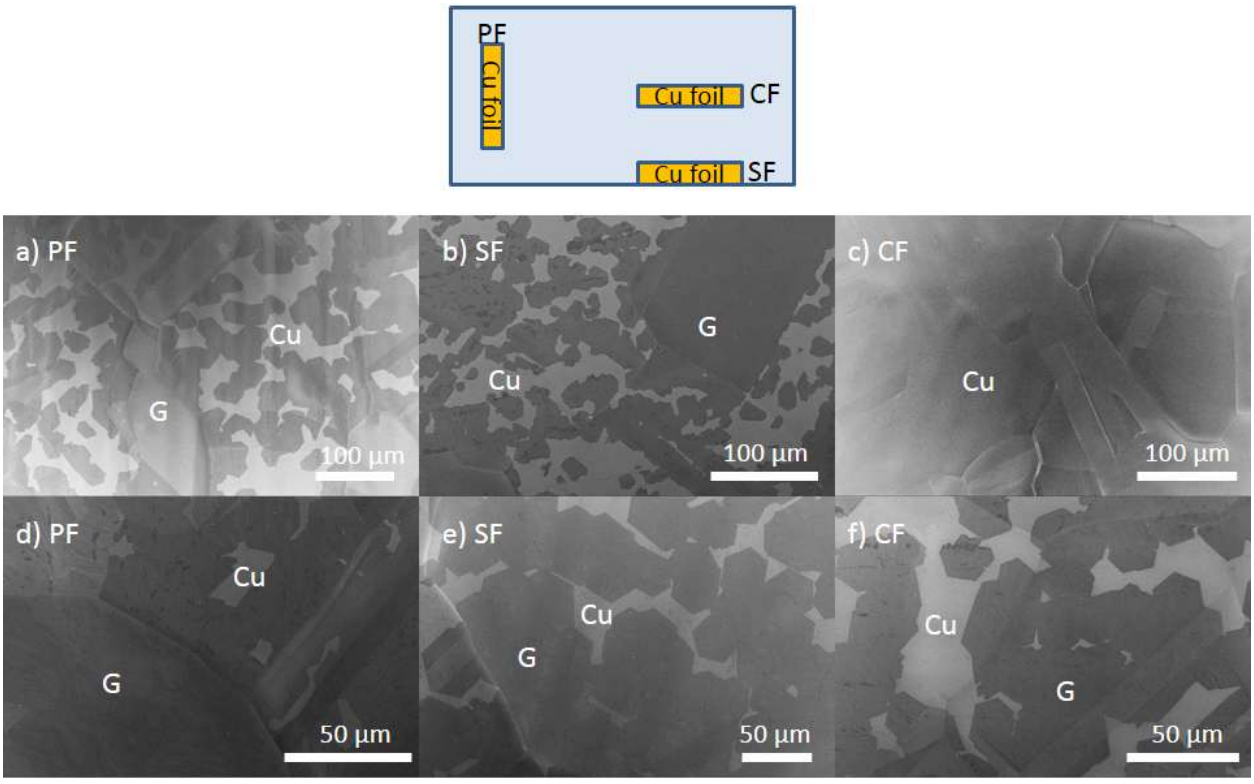


Figure S4. Orientation dependence of growth at atmospheric pressure and *T*=1000 °C for samples oriented perpendicular to the flow (PF), oriented parallel to the flow located on the inner surface of the process quartz tube (SF), and oriented parallel to the flow located in the center of the tube (CF), for a-c) 18 ppm $CH_4$ and d-f) 19 ppm $CH_4$. The CMC of PF and SF samples is 18 ppm, while the CMC of the CF sample is 19 ppm.

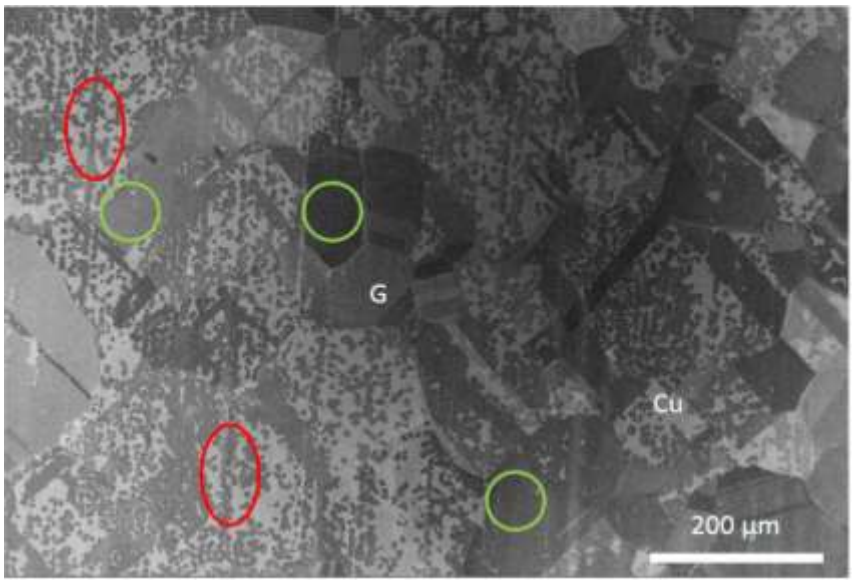


Figure S5. CMC growth (18 ppm $CH_4$) at atmospheric pressure showing preferential coverage on some Cu crystal facets (green circles) and ridges in Cu foil (red circles).

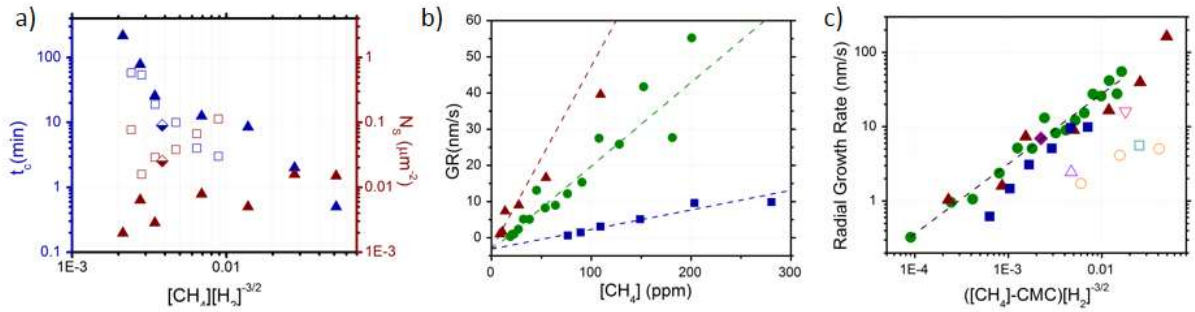


Figure S6. a) $t_c$ (blue symbols, left axis) and $N_S$ (red symbols, right axis) for $[H_2]_{(g)}$=2.5, 10, and 20% (filled triangles, open squares, half-filled diamonds, respectively), b) $[CH_4]_{(g)}$ dependence of radial growth rate ($1/N_S^{1/2}t_c$) for $[H_2]_{(g)}$ = 2.5, 5, and 10 % as red triangles, green circles, and blue squares, respectively (linear scale), c) BU supersaturation dependence of radial growth rate ($1/N_S^{1/2}t_c$) for this work (closed symbols): $[H_2]_{(g)}$ = 2.5, 5, and 10 % same as (b) and $[H_2]_{(g)}$ = 20 % purple diamonds, and other AP-CVD literature at $T$=1000°C (open symbols): pink downward triangles,[15] orange circles,[16] teal squares,[17] and violet upward triangles.[18]

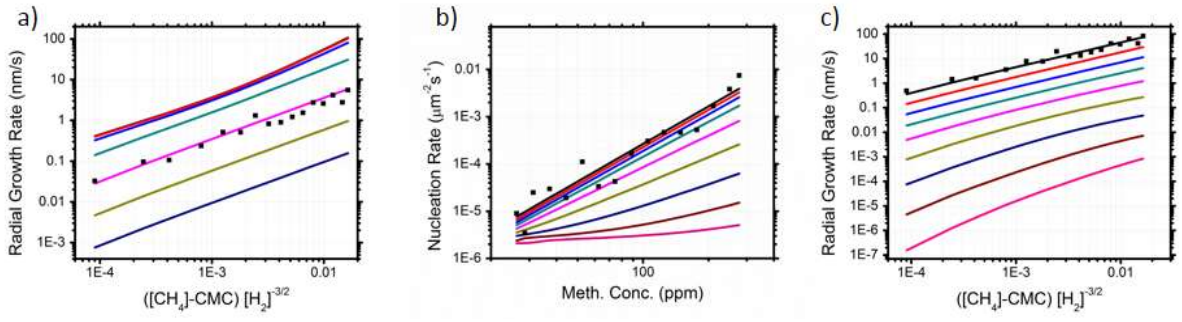


Figure S7. a) Simulated Radial Growth Rate ($1/N_S^{1/2}t_c$) for transition between CC and LC capture, with $E_D$= 0, 0.2, 0.4, 0.6, 0.8, 1, 1.2 eV (black, red, blue, teal, pink, yellow, navy), experimental data as black squares, see text for details. Simulated b) Nucleation Rate ($N_S/t_c$) and c) Radial Growth Rate ($1/N_S^{1/2}t_c$) for transition between CLC and ALC concentrations, with $K_A$= 1, 1.2, 1.4, 1.6, 1.8, 2, 2.2, 2.4, 2.6 eV (black, red, blue, teal, pink, yellow, navy, brown, magenta), experimental data as black squares, see text for details.

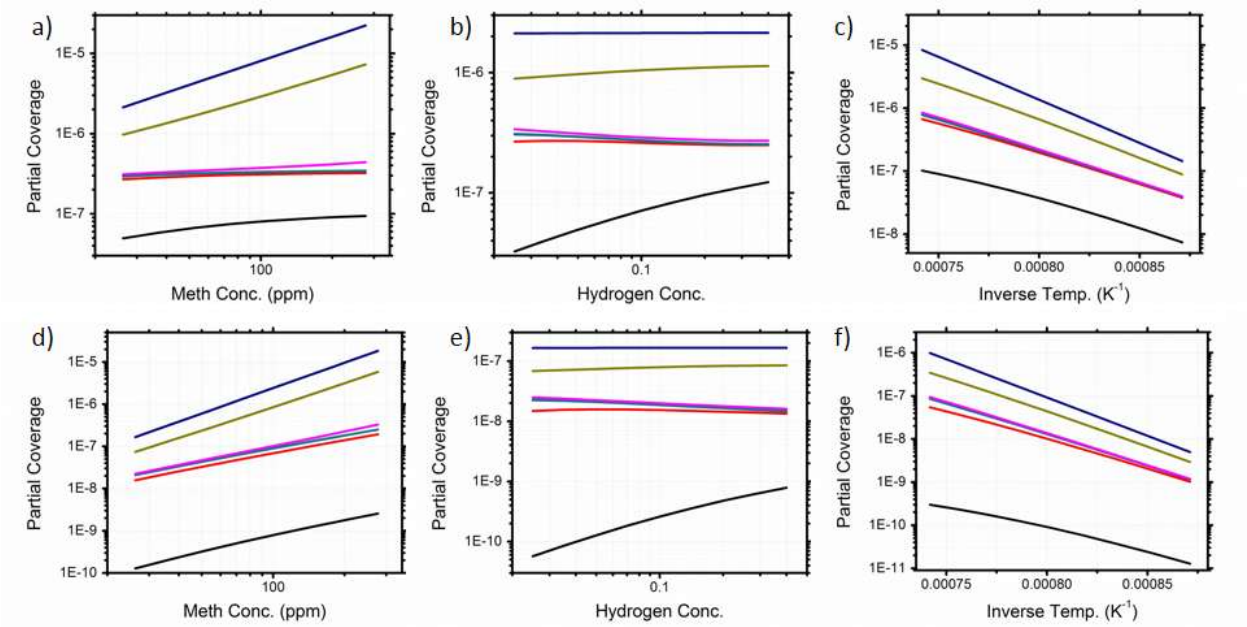


Figure S8. Simulated surface concentrations including desorption of intermediates. a) CH as a function of $[CH_4]_{(g)}$, b) CH as a function of $[H_2]_{(g)}$ with $[CH_4]_{(g)} \propto [H_2]_{(g)}^{3/2}$, c) CH as a function of $T$, d) C-CH as a function of $[CH_4]_{(g)}$, e) C-CH as a function of $[H_2]_{(g)}$ with $[CH_4]_{(g)} \propto [H_2]_{(g)}^{3/2}$, f) C-CH as a function of $T$. The kinetic barrier for desorption of all species = 0, 0.5, 1, 1.5, 2, 2.5, 3 eV (black, red, blue, teal, pink, yellow, navy), see text for details.

## XI. Supporting References:


1. J. Frenkel, *Zeitschrift für Physik A Hadrons and Nuclei*, 1924, **26**, 117-138.
2. G. Zinsmeister, *Vacuum*, 1966, **16**, 529-535.
3. B. Lewis and J. C. Anderson, *Nucleation and Growth of Thin Films*, Academic Press, London, UK, 1978.
4. J. A. Venables, G. D. T. Spiller and M. Hanbucken, *Reports on Progress in Physics*, 1984, **47**, 399.
5. B. Lewis and V. Halpern, *Journal of Crystal Growth*, 1976, **33**, 39-52.
6. A. Zangwill and D. D. Vvedensky, *Nano Letters*, 2011, **11**, 2092-2095.
7. W. Zhang, P. Wu, Z. Li and J. Yang, *The Journal of Physical Chemistry C*, 2011, **115**, 17782-17787.
8. D. Walton, *Journal of Chemical Physics*, 1962, **37**, 2182.
9. X. Mi, V. Meunier, N. Koratkar and Y. F. Shi, *Physical Review B*, 2012, **85**.
10. H. Shu, X. Chen, X. Tao and F. Ding, *Acs Nano*, 2012, **6**, 3243-3250.
11. Y. Hao, M. S. Bharathi, L. Wang, Y. Liu, H. Chen, S. Nie, X. Wang, H. Chou, C. Tan and B. Fallahazad, *Science*, 2013, 1243879.
12. P. Koskinen, S. Malola and H. Häkkinen, *Physical Review Letters*, 2008, **101**, 115502.
13. A. V. Zeigarnik, R. E. Valdes-Perez and O. N. Myatkovskaya, *The Journal of Physical Chemistry B*, 2000, **104**, 10578-10587.
14. K. Hayashi, S. Sato, M. Ikeda, C. Kaneta and N. Yokoyama, *Journal of the American Chemical Society*, 2012, **134**, 12492-12498.
15. Y. A. Wu, A. W. Robertson, F. Schäffel, S. C. Speller and J. H. Warner, *Chemistry of Materials*, 2011, **23**, 4543-4547.
16. I. Vlassiouk, M. Regmi, P. Fulvio, S. Dai, P. Datskos, G. Eres and S. Smirnov, *ACS Nano*, 2011, **5**, 6069-6076.
17. J. Zhang, P. Hu, X. Wang, Z. Wang, D. Liu, B. Yang and W. Cao, *Journal of Materials Chemistry*, 2012, **22**, 18283-18290.
18. Z. Luo, S. Kim, N. Kawamoto, A. M. Rappe and A. T. C. Johnson, *Acs Nano*, 2011, **5**, 9154-9160.